

DisReserv (v1.0): Analytical displacement solution due to reservoir compaction with arbitrary geometry and under arbitrary pressure changes

Valeria C. F. Barbosa¹, Vanderlei C. Oliveira Jr.¹, and Andre D. Arelaro^{1,2}

¹Department of Geophysics, Observatório Nacional, Rio de Janeiro, Brazil

²PETROBRAS, Rio de Janeiro, Brazil

Correspondence: Valeria C. F. Barbosa (valcris@on.br)

Abstract. We have presented analytical solutions for the displacement due to reservoir compaction with arbitrary geometry and under arbitrary pressure changes. These solutions are based on the similarity between the gravitational potential yielded by a volume source under a density variation and the thermoelastic displacement potential yielded by a volume source in a half-space under a pressure variation. This similarity enables the use of closed expressions of the gravitational potential and its derivatives for calculating the displacement and stress fields due to a volume source under a pressure variation. We discretized the reservoir as a grid of 3D right rectangular prisms juxtaposed in the horizontal and vertical directions. Each prism has homogeneous pressure; however, pressure variations among different prisms are allowed. This parametrization of the reservoir yields a piecewise-constant distribution of pressure in the subsurface. The discrete reservoir modeling to calculate the displacement and stress fields due to this pressure variation follows the nucleus-of-strain concept. The nucleus of strain is considered an infinitesimal reservoir volume element. The displacement and stress fields due each prism are calculated by integrating the nucleus of strain over the volume of the prism. Finally, the displacement and stress due to the reservoir are computed by the sum of the contributions of each prism. We provide a Python implementation (DisReserv) of our method to calculate the displacement and stress fields due to a reservoir with arbitrary shape and distribution of pressure changes. Our expressions are valid both inside and outside the reservoir. We calculate the displacement and stress fields in three scenarios: i) cylindrical reservoir under uniform depletion; ii) cylindrical reservoir under non uniform depletion and iii) reservoir with arbitrary geometry and under arbitrary pressure distribution. The results obtained for the three scenarios show that our method produces null stress field components at the free surface.

Copyright statement.

1 Introduction

The surface subsidence due to oil or gas withdrawal from a reservoir in the subsurface may occur as a result of geomechanical changes caused by pressure drop. The phenomenon of subsidence by fluid extraction has been observed in a variety of oil fields,

e.g., the Ekofisk field, southern North Sea (Borges et al., 2020) and the Groningen gas field in the northeast Netherlands (van Thienen-visser and Fokker, 2017). Because the subsidence close to hydrocarbon fields under production can induce earthquakes (e.g., Dahm et al., 2015; Grigoli et al., 2017), the petroleum companies have been an increased interest in monitoring the magnitude and distribution of subsidence resulting from reservoir depletion. The subsidence monitoring is accomplished by means of calculating the displacement field for a given set of reservoir properties.

The possibility of occurrence of catastrophic events, related to subsidence due to extraction or injection of fluids in reservoir, has stimulated efforts to develop analytical methods for modeling the displacement and stress fields due to reservoir compaction. The physical foundation of the displacement, stress and strain fields in the subsurface due to a reduction of pressure in the reservoir comes from the theory of thermoelasticity. Theory of thermoelasticity has been laid in the first half of the nineteenth century to describe the interaction between the thermal field and elastic bodies. In the uncoupled thermoelasticity theory for quasi-static problems (i.e., problems with negligible inertia effects), Goodier (1937) employed the method of superposition using displacement potential functions and introduced the concept of nucleus of thermoelastic strain in an infinite space. Specifically, Goodier's (1937) method simplified the thermoelastic problem by replacing it by an isothermal elastic problem with different boundary conditions together with the solution of a Poisson's equation (Tao, 1971). Mindlin and Cheng (1950) and Sen (1951) extended the Goodier's method to a homogenous half-space. Sharma (1956) deduced the displacement and stress fields in an infinite elastic plate due to a nucleus of thermoelastic strain located at a point inside it by using infinite integrals involving Bessel functions.

The subsidence resulting from reservoir depletion is in the context of poroelastic theory. Geertsma (1957) remarked the analogy between the theories of thermoelasticity and poroelasticity. To our knowledge, Geertsma (1973) was the first to solve the poroelastic problem by using the nucleus-of-strain concept in the half-space, which in turn was proposed by Mindlin and Cheng (1950) and Sen (1951) in the theory of thermoelasticity. Geertsma (1973) derived analytical expressions for the stress and displacement fields for a thin disk-shaped reservoir. Segall (1992) followed Geertsma (1973) and extended the analytical solutions of the displacement and stress fields assuming general axisymmetric geometries and an arbitrary radial pressure distribution.

Geertsma and van Opstal (1973) applied the nucleus-of-strain concept in the half-space to calculate the spatial subsidence distribution due to the production of reservoir with an arbitrary 3D shape. By assuming a producing reservoir embedded in an a homogeneous, isotropic, and elastic medium, and a reservoir model in which the pressure perturbations are related to the displacement field by a linear relationship, Geertsma and van Opstal (1973) discretized the reservoir into a grid of prisms and calculated the displacement due to the pressure change in the whole reservoir by the superposition of the displacement due to the constant pressure change in each prism. Tempone et al. (2010) adopted the same reservoir model used in Geertsma and van Opstal (1973) and extended the nucleus-of-strain concept in the half-space to consider the effects of a rigid basement. Similarly, Tempone et al. (2010) assumed a reservoir embedded in an a homogeneous, isotropic, and elastic medium and calculated the displacement, stress and strain fields subject to uniform depletion. The main drawbacks in Geertsma and van Opstal (1973) and Tempone et al. (2010) are the assumption of homogeneous reservoir and the solution is only valid outside the reservoir. In

this case, the displacements within the reservoir are calculated by a linear interpolation of the displacements at the upper and lower edges of the reservoir (Tempone et al., 2012).

Considering an inhomogeneous poroelastic model consists of layered stratigraphy, Mehrabian and Abousleiman (2015) developed closed-form formulae for the displacement and stress fields outside and inside of the reservoir embedded within elastic strata with different mechanical properties and subjected to pore pressure disturbances due to fluid extraction or injection. By assuming a linear elastic semi-infinite medium, Muñoz and Roehl (2017) developed analytical solution for the displacement field outside and inside of an arbitrarily-shaped reservoir under arbitrary distribution of pressure changes. Muñoz and Roehl (2017) parametrized the reservoir into a grid of 3D prisms and used the nucleus-of-strain concept. The nucleus of strain is taking as an infinitesimal volume element for each prism and the displacement solution due to each prism is obtained by a three-dimensional integration over the prism volume. The displacement field outside and inside of the reservoir is given by the summation of the displacement fields of the displacements produced by all prisms setting up the reservoir model.

The present work assumes a linear elastic semi-infinite medium and provides an analytical solution for displacement field due to an arbitrarily-shaped reservoir under arbitrary distribution of pressure changes. Like Muñoz and Roehl (2017) we used the nucleus-of-strain concept and discretized the reservoir into a grid of 3D prisms along the x -, y - and $-z$ directions. We also consider the nucleus of strain as an infinitesimal volume element for each prism and the displacement solution due to each prism is obtained by a three-dimensional integration over the prism volume. The final displacement field due to the whole reservoir is the sum of the displacements produced by the prisms. In contrast with Muñoz and Roehl (2017)'s method we take advantage the similarity between the equations for calculating the displacement field due to a volume source in a half-space under a pressure variation and the gravitational potential due to a volume source under a density variation. This similarity makes possible the use of closed expressions of the gravitational potential and its derivatives produced by the 3D right rectangular prism derived by Nagy et al. (2000) and (2002) and Fukushima (2020) for calculating the displacement field due to a volume source under a pressure variation. The adopted exact analytical formulae of the gravitational field are valid expressions either outside or inside the prisms because the implemented expressions make use of modified arctangent function proposed by Fukushima (2020). We present routines written in Python language (Python 3.7.6) to calculate the displacement fields due to a reservoir with arbitrary shape and distribution of pressure changes. We validate our equations by verifying that at the free surface the stress fields are null. Tests with synthetic data validate our approach.

2 THEORY

The displacement, stress and strain fields in the subsurface caused by reservoir compaction due to hydrocarbon production are grounded on the theory of thermoelasticity.

The Goodier's thermoelastic displacement potential ϕ satisfies the Poisson's equation (Goodier, 1937), i.e.:

$$\nabla^2 \phi = m T, \quad (1)$$

where ∇^2 is the Laplacian operator, T is the temperature variation and

$$m = \alpha \frac{1 + \nu}{1 - \nu}, \quad (2)$$

where α is the coefficient of linear thermal expansion and ν is the Poisson's ratio.

90 From the potential theory, a particular solution of equation 1 is

$$\phi(x, y, z) = -\frac{m}{4\pi} \int_v \int \int \frac{T(x', y', z')}{\sqrt{(x - x')^2 + (y - y')^2 + (z - z')^2}} dv', \quad (3)$$

where $\phi(x, y, z)$ represents the Newtonian gravitational potential (Kellogg, 1929) that would be produced at the coordinates x, y and z by a continuous density distribution $-\frac{m}{4\pi} T(x', y', z')$. The integral in equation 3 is conducted over the coordinates x', y' and z' , denoting, respectively, the $x-$, $y-$ and $-z$ coordinates of an arbitrary point belonging to the interior of the volume

95 v of the solid.

From equation 3 and the potential theory, Goodier (1937) showed that, if an element of volume dv in the infinite solid is at a temperature $T(x', y', z')$, the remainder being at temperature zero, the displacement vector \mathbf{u} caused by this temperature is the gradient of the Goodier's thermoelastic displacement potential, i.e.,

$$\mathbf{u} = \nabla \phi(x, y, z), \quad (4)$$

100 where ∇ is the gradient operator.

To a homogenous half-space, Mindlin and Cheng (1950) showed that the method proposed by Goodier (1937) can be extended by the displacement solution given by:

$$\mathbf{u} = \nabla \phi_1 + \nabla_2 \phi_2, \quad (5)$$

where $\phi_1 \equiv \phi_1(x, y, z)$ is the potential defined in equation 3, $\phi_2 \equiv \phi_2(x, y, z)$ is defined as "image potential" (Segall, 1992)

105 due to a image point at the coordinates $(x', y', -z')$ and the operator ∇_2 is expressed by

$$\nabla_2 = (3 - 4\nu)\nabla + 2\nabla z \frac{\partial}{\partial z} - 4(1 - \nu)\hat{\mathbf{z}}\nabla_z^2, \quad (6)$$

where $\hat{\mathbf{z}}$ is the unit vector in the z -direction and ∇_z^2 is a scalar operator in which the operand is firstly multiplied by z and then operated upon by the Laplacian ∇^2 .

Equation 5 is the displacement solution for the variation of temperature due to a single nucleus of strain buried at depth z'
110 in a semi-infinite homogeneous medium. In the right hand side of equation 5, the first term $\nabla \phi_1$ represents the displacement in an infinite medium, and the second term represents a correction of the displacement due a half-space, also known as "image nucleus solution".

3 METHODOLOGY

Let's assume that a reservoir in the interior of the Earth is subject to a compaction due to hydrocarbon production. The
115 compaction is caused by the pressure change within the reservoir, which in turn causes a surface subsidence (or surface

displacement). Here, we use a Cartesian coordinate system with the x -axis pointing to north, the y -axis pointing to east and the z -axis pointing downward. We discretize the reservoir into an $m_x \times m_y \times m_z$ grid of 3D vertical juxtaposed prisms ($m_x \cdot m_y \cdot m_z = M$) along the x , y and z axes, respectively, in which the pressure within each prism is assumed to be constant and known. Each prism in the reservoir model may undergo a distinct pressure change. The subsidence effect is the displacement field due to the pressure change throughout the reservoir and is calculated by the sum of the displacement produced by each prism.

The discrete forward modeling to calculate the displacement and stress fields due to a piecewise-constant distribution of the pressure contrast within a reservoir follows the nucleus-of-strain approach. We assume that a nucleus of strain represents an infinitesimal reservoir volume element. The displacement solution for a single nucleus of strain in a homogeneous elastic semi-infinite medium (equation 5) will be used as an element of the displacement. Then we calculate the displacement field due to the pressure contrast of a prism by integrating the nucleus of strain over its volume. The same approach is used to compute the stress field due to a prism.

3.1 The discrete forward modeling due to a nucleus of strain in a homogeneous elastic semi-infinite medium

By considering the discrete form of equation 5, the displacement vector $\mathbf{u}_{ij} \equiv \mathbf{u}(x_i, y_i, z_i, x'_j, y'_j, z'_j)$ at an arbitrary point (x_i, y_i, z_i) due to the j th nucleus of strain at the coordinates (x'_j, y'_j, z'_j) will be calculated by

$$\mathbf{u}_{ij} = \mathbf{u}_{1ij} + \mathbf{u}_{2ij}, \quad (7)$$

where \mathbf{u}_{1ij} is the displacement vector at the point (x_i, y_i, z_i) due to the j th single nucleus in the infinite space and \mathbf{u}_{2ij} is the correction of the displacement considering a semi-space (image nucleus solution). The term \mathbf{u}_{1ij} (equation 7) is given by

$$\mathbf{u}_{1ij} = \frac{A(1+\nu)}{E} \nabla \left(\frac{1}{R_{1ij}} \right) \Delta p_j dv'_j \quad (8)$$

and represents the gradient of the potential

$$\phi_1 = -\frac{C_m}{4\pi} \frac{\Delta p_j dv'_j}{R_{1ij}}. \quad (9)$$

The term \mathbf{u}_{2ij} (equation 7) is given by

$$\mathbf{u}_{2ij} = \frac{A(1+\nu)}{E} \left[(3-4\nu) \nabla \left(\frac{1}{R_{2ij}} \right) + 2 \nabla \left(z \frac{\partial}{\partial z} \frac{1}{R_{2ij}} \right) - 4(1-\nu) \hat{\mathbf{z}} \nabla^2 \left(\frac{z}{R_{2ij}} \right) \right] \Delta p_j dv'_j \quad (10)$$

and is obtained by applying the operator ∇_2 (equation 6) to the image potential

$$\phi_2 = -\frac{C_m}{4\pi} \frac{\Delta p_j dv'_j}{R_{2ij}}. \quad (11)$$

In equations 8–11, all derivatives are computed with respect to the coordinates of the point (x_i, y_i, z_i) , Δp_j is the pressure contrast of the j th nucleus, dv'_j is an infinitesimal element of volume centered at the j th nucleus of strain (x'_j, y'_j, z'_j) , A is the constant

$$A = -\frac{C_m E}{4\pi(1+\nu)}, \quad (12)$$

145 C_m is the uniaxial compaction coefficient (see Geertsma, 1966; Tempone et al., 2010 and Muñoz and Roehl, 2017)

$$C_m = \frac{1}{E} \frac{(1+\nu)(1-2\nu)}{(1-\nu)}, \quad (13)$$

and E is the Young's modulus. In equation 9, R_{1ij} is the distance from the i th point (x_i, y_i, z_i) to the j th nucleus of strain (x'_j, y'_j, z'_j) , i.e.:

$$R_{1ij} = \sqrt{(x_i - x'_j)^2 + (y_i - y'_j)^2 + (z_i - z'_j)^2}. \quad (14)$$

150 In equation 11, R_{2ij} is the distance from the i th point (x_i, y_i, z_i) to the j th image nucleus $(x'_j, y'_j, -z'_j)$, i.e.:

$$R_{2ij} = \sqrt{(x_i - x'_j)^2 + (y_i - y'_j)^2 + (z_i + z'_j)^2}. \quad (15)$$

Figure 1 shows a schematic representation of the geometry of the nucleus of strain problem in a semi-infinite medium. The horizontal plane $z = 0$ is called "free surface". The x -, y - and z -components of the vectors \mathbf{u}_{1ij} (equation 8) and \mathbf{u}_{2ij} (equation 10) can be explicitly defined as follows:

$$155 \quad \mathbf{u}_{1ij} = \frac{A(1+\nu)}{E} \begin{bmatrix} \frac{\partial}{\partial x} \frac{1}{R_{1ij}} \\ \frac{\partial}{\partial y} \frac{1}{R_{1ij}} \\ \frac{\partial}{\partial z} \frac{1}{R_{1ij}} \end{bmatrix} \Delta p_j dv'_j \quad (16)$$

and

$$\mathbf{u}_{2ij} = \frac{A(1+\nu)}{E} \left\{ (3-4\nu) \begin{bmatrix} \frac{\partial}{\partial x} \frac{1}{R_{2ij}} \\ \frac{\partial}{\partial y} \frac{1}{R_{2ij}} \\ -\frac{\partial}{\partial z} \frac{1}{R_{2ij}} \end{bmatrix} + 2 z_i \begin{bmatrix} \frac{\partial^2}{\partial x \partial z} \frac{1}{R_{2ij}} \\ \frac{\partial^2}{\partial y \partial z} \frac{1}{R_{2ij}} \\ \frac{\partial^2}{\partial z^2} \frac{1}{R_{2ij}} \end{bmatrix} \right\} \Delta p_j dv'_j. \quad (17)$$

By following Sharma (1956) and Tempone et al. (2010), the stress vector $\boldsymbol{\sigma}_{ij} \equiv \boldsymbol{\sigma}(x_i, y_i, z_i, x'_j, y'_j, z'_j)$ at the point (x_i, y_i, z_i) due to the j th single nucleus of strain buried in the half space is given by

$$160 \quad \boldsymbol{\sigma}_{ij} = \boldsymbol{\sigma}_{1ij} + \boldsymbol{\sigma}_{2ij}, \quad (18)$$

where $\boldsymbol{\sigma}_{1ij} \equiv \boldsymbol{\sigma}_1(x_i, y_i, z_i, x'_j, y'_j, z'_j)$ is the stress vector at the point (x_i, y_i, z_i) due to the j th single nucleus in the infinite space and $\boldsymbol{\sigma}_{2ij} \equiv \boldsymbol{\sigma}_2(x_i, y_i, z_i, x'_j, y'_j, z'_j)$ is the stress vector at the point (x_i, y_i, z_i) that gives the correction of the stress due to the j th image nucleus considering a semi-space. These two vectors are given by

$$\boldsymbol{\sigma}_{1ij} = A \begin{bmatrix} \frac{\partial^2}{\partial x \partial z} \frac{1}{R_{1ij}} \\ \frac{\partial^2}{\partial y \partial z} \frac{1}{R_{1ij}} \\ \frac{\partial^2}{\partial z^2} \frac{1}{R_{1ij}} \end{bmatrix} \Delta p_j dv'_j, \quad (19)$$

165 and

$$\boldsymbol{\sigma}_{2ij} = A \left\{ \begin{bmatrix} \frac{\partial^2}{\partial x \partial z} \frac{1}{R_{2ij}} \\ \frac{\partial^2}{\partial y \partial z} \frac{1}{R_{2ij}} \\ -\frac{\partial^2}{\partial z^2} \frac{1}{R_{2ij}} \end{bmatrix} + 2 z_i \begin{bmatrix} \frac{\partial^3}{\partial x \partial z^2} \frac{1}{R_{2ij}} \\ \frac{\partial^3}{\partial y \partial z^2} \frac{1}{R_{2ij}} \\ \frac{\partial^3}{\partial z^3} \frac{1}{R_{2ij}} \end{bmatrix} \right\} \Delta p_j dv'_j. \quad (20)$$

According to Sharma (1956) and Tempone et al. (2010), the Beltrami's equations (Beltrami, 1902–1920) and the equilibrium equations must be satisfied to obtain the contribution of the stress field in the half space. Additionally, the boundary condition $\sigma_{ij} = \mathbf{0}$ (equation 18), where $\mathbf{0}$ is the zero vector, must be satisfied at the free surface ($z_i = 0$). This condition can be easily verified by adding the vectors σ_{1ij} (equation 19) and σ_{2ij} (equation 20) computed at any point on the free surface ($x_i, y_i, z_i = 0$).

3.2 The discrete displacement forward modeling due to a reservoir in a homogeneous elastic semi-infinite medium

We parameterize the reservoir as a grid of juxtaposed right rectangular prisms. Each grid prism has a constant pressure contrast Δp_j ; however, pressure variations among different prisms are allowed. To calculate the displacement field produced by the j th prism at the i th coordinates (x_i, y_i, z_i) , we integrate the solution deduced for a single nucleus of strain (equation 7) over its volume and obtain

$$\tilde{\mathbf{u}}_{ij} = \iiint_{v_{1j}} \mathbf{u}_{1ij} dv'_j + \iiint_{v_{2j}} \mathbf{u}_{2ij} dv'_j, \quad (21)$$

where both integrals are conducted with respect to the variables (x'_j, y'_j, z'_j) . The first integral in equation 21 is conducted over the volume v_{1j} of the j th prism and the second is conducted over the volume v_{2j} of a different prism symmetrically positioned above the free surface and conveniently called j th "image prism". Volume v_{1j} is defined by $x_{1j}, x_{2j}, y_{1j}, y_{2j}, z_{1j}$, and z_{2j} , which represent, respectively, the south, north, west, east, top, and bottom borders of the j th prism. Volume v_{2j} of the j th image prism is defined in a similar way, but with top and bottom given by $z_{1j} - 2z_{cj}$ and $z_{2j} - 2z_{cj}$, where $z_{cj} = \frac{1}{2}(z_{1j} + z_{2j})$ is the center depth of the j th prism.

The total displacement vector at the point (x_i, y_i, z_i) due to the pressure change in the whole reservoir is defined as the sum of the displacements \mathbf{u}_{ij} (equation 21) yielded by each prism with constant pressure Δp_j :

$$\tilde{\mathbf{u}}_i = \sum_{j=1}^M \tilde{\mathbf{u}}_{ij}, \quad (22)$$

where M is the number of prisms setting up the reservoir model. The horizontal component of the total displacement vector $\tilde{\mathbf{u}}_i$ (equation 22) is calculated by

$$\tilde{u}_{i_h} = \sqrt{\tilde{u}_{i_x}^2 + \tilde{u}_{i_y}^2}, \quad (23)$$

where \tilde{u}_{i_x} and \tilde{u}_{i_y} are the x - and y - components.

By substituting equations 16 and 17 into equation 21, we obtain

$$\tilde{u}_{ij_\alpha} = \frac{A(1+\nu)}{E} \Delta p_j \left[\iiint_{v_{1j}} \frac{\partial}{\partial \alpha} \frac{1}{R_{1ij}} dv'_j + (3-4\nu) \iiint_{v_{2j}} \frac{\partial}{\partial \alpha} \frac{1}{R_{2ij}} dv_j + 2z_i \iiint_{v_{2j}} \frac{\partial^2}{\partial \alpha \partial z} \frac{1}{R_{2ij}} dv'_j \right], \quad (24)$$

where $\alpha = x, y$, and

$$\tilde{u}_{ij_z} = \frac{A(1+\nu)}{E} \Delta p_j \left[\iiint_{v_{1j}} \frac{\partial}{\partial z} \frac{1}{R_{1ij}} dv'_j - (3-4\nu) \iiint_{v_{2j}} \frac{\partial}{\partial z} \frac{1}{R_{2ij}} dv'_j + 2z_i \iiint_{v_{2j}} \frac{\partial^2}{\partial z^2} \frac{1}{R_{2ij}} dv'_j \right]. \quad (25)$$

- 195 In the right-hand side of equations 24 and 25, the three integrals have the same form of derivatives of the gravitational potential produced by the j th prism and image prism. The first integral corresponds to the α -component of the gravitational attraction produced by the j th prism. The second and third integrals correspond, respectively, to the α -component of the gravitational attraction and to the αz -component of the gravitational gradient tensor produced by the j th image prism. The similarity between the displacement fields due to a volume source in a half-space and the gravitational field allows the use of closed
200 expressions of the gravitational potential and its derivatives produced by the 3D right rectangular prism.

In equations 24 and 25, the integrals depending on first derivatives of $\frac{1}{R_{1ij}}$ have the following closed solutions (Nagy et al., 2000, 2002):

$$\int_{x_{1j}}^{x_{2j}} \int_{y_{1j}}^{y_{2j}} \int_{z_{1j}}^{z_{2j}} \frac{\partial}{\partial x} \frac{1}{R_{1ij}} dv'_j = \left| \left| \left| y \ln(z+R) + z \ln(y+R) - x \tan^{-1} \left(\frac{yz}{xR} \right) \right|_{X_{1j}}^{X_{2j}} \right|_{Y_{1j}}^{Y_{2j}} \right|_{Z_{1j}}^{Z_{2j}}, \quad (26)$$

$$205 \int_{x_{1j}}^{x_{2j}} \int_{y_{1j}}^{y_{2j}} \int_{z_{1j}}^{z_{2j}} \frac{\partial}{\partial y} \frac{1}{R_{1ij}} dv'_j = \left| \left| \left| x \ln(z+R) + z \ln(x+R) - y \tan^{-1} \left(\frac{xz}{yR} \right) \right|_{X_{1j}}^{X_{2j}} \right|_{Y_{1j}}^{Y_{2j}} \right|_{Z_{1j}}^{Z_{2j}}, \quad (27)$$

and

$$\int_{x_{1j}}^{x_{2j}} \int_{y_{1j}}^{y_{2j}} \int_{z_{1j}}^{z_{2j}} \frac{\partial}{\partial z} \frac{1}{R_{1ij}} dv'_j = \left| \left| \left| x \ln(y+R) + y \ln(x+R) - z \tan^{-1} \left(\frac{xy}{zR} \right) \right|_{X_{1j}}^{X_{2j}} \right|_{Y_{1j}}^{Y_{2j}} \right|_{Z_{1j}}^{Z_{2j}}, \quad (28)$$

where all derivatives are computed with respect to the coordinates of the i th point (x_i, y_i, z_i) , $R = \sqrt{x^2 + y^2 + z^2}$, and

$$\begin{aligned} X_{1j} &= x_i - x_{1j} \\ X_{2j} &= x_i - x_{2j} \\ Y_{1j} &= y_i - y_{1j} \\ Y_{2j} &= y_i - y_{2j} \\ Z_{1j} &= z_i - z_{1j} \\ Z_{2j} &= z_i - z_{2j} \end{aligned} \quad . \quad (29)$$

- 210 The remaining integrals, in the right-hand side of equations 24 and 25, depend on first and second derivatives of $\frac{1}{R_{2ij}}$. These integrals are conducted over the volume v_{2j} of the j th image prism and have the following closed solutions (Nagy et al., 2000, 2002):

$$\int_{x_{1j}}^{x_{2j}} \int_{y_{1j}}^{y_{2j}} \int_{z_{1j}-2z_c}^{z_{2j}-2z_c} \frac{\partial}{\partial x} \frac{1}{R_{2ij}} dv'_j = \left| \left| \left| y \ln(z+R) + z \ln(y+R) - x \tan^{-1} \left(\frac{yz}{xR} \right) \right|_{X_{1j}}^{X_{2j}} \right|_{Y_{1j}}^{Y_{2j}} \right|_{Z_{1j}}^{Z_{2j}}, \quad (30)$$

$$215 \quad \int_{x_{1j}}^{x_{2j}} \int_{y_{1j}}^{y_{2j}} \int_{z_{1j}-2z_c}^{z_{2j}-2z_c} \frac{\partial}{\partial y} \frac{1}{R_{2ij}} dv'_j = \left| \left| \left| x \ln(z+R) + z \ln(x+R) - y \tan^{-1} \left(\frac{xz}{yR} \right) \right|_{X_{1j}}^{X_{2j}} \right|_{Y_{1j}}^{Y_{2j}} \right|_{Z_{1j}}^{Z_{2j}}, \quad (31)$$

$$\int_{x_{1j}}^{x_{2j}} \int_{y_{1j}}^{y_{2j}} \int_{z_{1j}-2z_c}^{z_{2j}-2z_c} \frac{\partial}{\partial z} \frac{1}{R_{2ij}} dv'_j = \left| \left| \left| x \ln(y+R) + y \ln(x+R) - z \tan^{-1} \left(\frac{xy}{zR} \right) \right|_{X_{1j}}^{X_{2j}} \right|_{Y_{1j}}^{Y_{2j}} \right|_{Z_{1j}}^{Z_{2j}}, \quad (32)$$

$$\int_{x_{1j}}^{x_{2j}} \int_{y_{1j}}^{y_{2j}} \int_{z_{1j}-2z_c}^{z_{2j}-2z_c} \frac{\partial^2}{\partial x \partial z} \frac{1}{R_{2ij}} dv'_j = \left| \left| \left| \ln(y+R) \right|_{X_{1j}}^{X_{2j}} \right|_{Y_{1j}}^{Y_{2j}} \right|_{Z_{1j}}^{Z_{2j}}, \quad (33)$$

220

$$\int_{x_{1j}}^{x_{2j}} \int_{y_{1j}}^{y_{2j}} \int_{z_{1j}-2z_c}^{z_{2j}-2z_c} \frac{\partial^2}{\partial y \partial z} \frac{1}{R_{2ij}} dv'_j = \left| \left| \left| \ln(x+R) \right|_{X_{1j}}^{X_{2j}} \right|_{Y_{1j}}^{Y_{2j}} \right|_{Z_{1j}}^{Z_{2j}}, \quad (34)$$

and

$$\int_{x_{1j}}^{x_{2j}} \int_{y_{1j}}^{y_{2j}} \int_{z_{1j}-2z_c}^{z_{2j}-2z_c} \frac{\partial^2}{\partial z \partial z} \frac{1}{R_{2ij}} dv'_j = \left| \left| \left| -\tan^{-1} \left(\frac{xy}{zR} \right) \right|_{X_{1j}}^{X_{2j}} \right|_{Y_{1j}}^{Y_{2j}} \right|_{Z_{1j}}^{Z_{2j}}. \quad (35)$$

In these integrals related to the j th image prism (equations 30–35), the integration limits along the z direction are given by

$$225 \quad \begin{aligned} Z_{1j} &= z_i - z_{1j} + 2z_{cj}, \\ Z_{2j} &= z_i - z_{2j} + 2z_{cj} \end{aligned}, \quad (36)$$

where $z_{cj} = \frac{1}{2}(z_{1j} + z_{2j})$ is the center depth of the j th prism. The remaining limits along x and y directions are the same defined by equation 29.

3.3 The discrete stress forward modeling due to a reservoir in a homogeneous elastic semi-infinite medium

By following the similar approach used in the previous subsection, the stress field of each prism assuming constant pressure is calculated by integrating solution for a nucleus of strain (equations 18, 19, and 20) over its volume. This integration leads to a stress vector $\tilde{\sigma}_{ij} \equiv \tilde{\sigma}(x_i, y_i, z_i, x'_j, y'_j, z'_j)$ given by

$$\tilde{\sigma}_{ij} = \iiint_{v_{1j}} \sigma_{1ij} dv'_j + \iiint_{v_{2j}} \sigma_{2ij} dv'_j, \quad (37)$$

where the first and second integrals are conducted, respectively, over the volumes v_{1j} and v_{2j} of the j th prism and the j th image prism. The total stress vector at the i th coordinates (x_i, y_i, z_i) due to the pressure change in the whole reservoir is calculated

235 by

$$\tilde{\sigma}_i = \sum_{j=1}^M \tilde{\sigma}_{ij}. \quad (38)$$

By substituting equation 19 and 20 into equation 37, we obtain the α -component (where $\alpha = x$ and y) and the z - component of the stress vector $\tilde{\sigma}_{ij}$ as follows:

$$\tilde{\sigma}_{ij_\alpha} = A \Delta p_j \left[\iiint_{v_{1j}} \frac{\partial^2}{\partial \alpha \partial z} \frac{1}{R_{1ij}} dv'_j + \iiint_{v_{2j}} \frac{\partial^2}{\partial \alpha \partial z} \frac{1}{R_{2ij}} dv'_j + 2 z_i \iiint_{v_{2j}} \frac{\partial^3}{\partial \alpha \partial z^2} \frac{1}{R_{2ij}} dv'_j \right] \quad (39)$$

240 and

$$\tilde{\sigma}_{ij_z} = A \Delta p_j \left[\iiint_{v_{1j}} \frac{\partial^2}{\partial z^2} \frac{1}{R_{1ij}} dv'_j + \iiint_{v_{2j}} \frac{\partial^2}{\partial z^2} \frac{1}{R_{2ij}} dv'_j + 2 z_i \iiint_{v_{2j}} \frac{\partial^3}{\partial z^3} \frac{1}{R_{2ij}} dv'_j \right]. \quad (40)$$

Similarly to the displacement field (equations 24 and 25), the three integrals in the right-hand side of equations 39 and 40 have the same form of derivatives of the gravitational potential produced by the j th prism and image prism. The integrals depending on $\frac{1}{R_{1ij}}$ have the following closed solutions (Nagy et al., 2000, 2002):

$$245 \quad \int_{x_{1j}}^{x_{2j}} \int_{y_{1j}}^{y_{2j}} \int_{z_{1j}}^{z_{2j}} \frac{\partial^2}{\partial x \partial z} \frac{1}{R_{1ij}} dv'_j = \left| \left| \ln(y + R) \right| \begin{array}{c} X_{2j} \\ X_{1j} \end{array} \right| \begin{array}{c} Y_{2j} \\ Y_{1j} \end{array} \left| \begin{array}{c} Z_{2j} \\ Z_{1j} \end{array} \right|, \quad (41)$$

$$\int_{x_{1j}}^{x_{2j}} \int_{y_{1j}}^{y_{2j}} \int_{z_{1j}}^{z_{2j}} \frac{\partial^2}{\partial y \partial z} \frac{1}{R_{1ij}} dv'_j = \left| \left| \ln(x + R) \right| \begin{array}{c} X_{2j} \\ X_{1j} \end{array} \right| \begin{array}{c} Y_{2j} \\ Y_{1j} \end{array} \left| \begin{array}{c} Z_{2j} \\ Z_{1j} \end{array} \right|, \quad (42)$$

and

$$\int_{x_{1j}}^{x_{2j}} \int_{y_{1j}}^{y_{2j}} \int_{z_{1j}}^{z_{2j}} \frac{\partial^2}{\partial z \partial z} \frac{1}{R_{1ij}} dv'_j = \left| \left| -\tan^{-1} \left(\frac{xy}{zR} \right) \right| \begin{array}{c} X_{2j} \\ X_{1j} \end{array} \right| \begin{array}{c} Y_{2j} \\ Y_{1j} \end{array} \left| \begin{array}{c} Z_{2j} \\ Z_{1j} \end{array} \right|, \quad (43)$$

250 where the limits X_{1j} , X_{2j} , Y_{1j} , Y_{2j} , Z_{1j} , and Z_{2j} are defined by equation 29. The integrals depending on second derivatives of $\frac{1}{R_{2ij}}$ in the right-hand side of equations 39 and 40 have closed solutions defined by equations 33, 34, and 35. Finally, the remaining integrals depending on third derivatives of $\frac{1}{R_{2ij}}$ have closed solutions given by (Nagy et al., 2000, 2002):

$$\int_{x_{1j}}^{x_{2j}} \int_{y_{1j}}^{y_{2j}} \int_{z_{1j}-2z_c}^{z_{2j}-2z_c} \frac{\partial^3}{\partial x \partial z^2} \frac{1}{R_{2ij}} dv'_j = \left| \left| \frac{-yz}{R} \left(\frac{1}{x^2+z^2} \right) \right| \begin{array}{c} X_{2j} \\ X_{1j} \end{array} \right| \begin{array}{c} Y_{2j} \\ Y_{1j} \end{array} \left| \begin{array}{c} Z_{2j} \\ Z_{1j} \end{array} \right|, \quad (44)$$

$$255 \quad \int_{x_{1j}}^{x_{2j}} \int_{y_{1j}}^{y_{2j}} \int_{z_{1j}-2z_c}^{z_{2j}-2z_c} \frac{\partial^2}{\partial y \partial z^2} \frac{1}{R_{2ij}} dv'_j = \left| \left| \frac{-xz}{R} \left(\frac{1}{y^2+z^2} \right) \right| \begin{array}{c} X_{2j} \\ X_{1j} \end{array} \right| \begin{array}{c} Y_{2j} \\ Y_{1j} \end{array} \left| \begin{array}{c} Z_{2j} \\ Z_{1j} \end{array} \right|, \quad (45)$$

$$\int_{x_{1j}}^{x_{2j}} \int_{y_{1j}}^{y_{2j}} \int_{z_{1j}}^{z_{2j}} \frac{\partial^3}{\partial z^3} \frac{1}{R_{2ij}} dv'_j = \left| \left| \left| \frac{xy}{R} \left(\frac{1}{x^2+z^2} + \frac{1}{y^2+z^2} \right) \right|_{X_{1j}}^{X_{2j}} \right|_{Y_{1j}}^{Y_{2j}} \right|_{Z_{1j}}^{Z_{2j}}, \quad (46)$$

where the limits X_{1j} , X_{2j} , Y_{1j} , and Y_{2j} , are defined by equation 29 and the limits Z_{1j} , and Z_{2j} by equation 36.

3.4 Computation notes

260 In equations 26–28, 30–35 and 41–43, we adopted the modifications proposed by Fukushima (2020). To overcome the zero division in evaluating the arguments of the arctangent function, Fukushima (2020) replaced $\tan^{-1}(\frac{S}{T})$ by

$$arctan2(S, T) = \begin{cases} atan(S/T) & \text{if } T \neq 0 \\ \pi/2 & \text{if } T = 0 \text{ and } S > 0 \\ -\pi/2 & \text{if } T = 0 \text{ and } S < 0 \\ 0 & \text{if } T = 0 \text{ and } S = 0 \end{cases} \quad (47)$$

Additionally, if the argument of the logarithm is less than 10^{-10} , the logarithm is replaced by zero; otherwise the logarithm is calculated regularly

265 **4 NUMERICAL APPLICATIONS**

4.0.1 Disk-shaped reservoir under uniform depletion

Embedded in a semi-infinite homogenous medium, we simulated a vertical cylinder-like reservoir (Figure 2) with a radius of 500 m and whose horizontal coordinates of its center along the north-south and east-west directions are 0 m and 0 m, respectively. The depths to the top and to the bottom of the simulated reservoir are 750 m and 850 m, respectively. The 270 reservoir is uniformly depleted by $\Delta p = -10$ MPa. The Young's modulus is 3300 (in MPa), the Poisson's coefficient is 0.25, and the uniaxial compaction coefficient C_m (equation 13) is $2.2525 \cdot 10^{-4}$ MPa $^{-1}$.

To apply our methodology, we discretized the cylinder along the x - and y - directions into an 20×20 grid of prisms. Hence, we totalized 400 prisms all of them centered at 800 m deep, with depths to the top and to the bottom at 750 m and 850 m and with pressure contrast Δp_j , $j = 1, \dots, 400$ equal to -10 MPa. To apply the Geertsma's method (Geertsma, 1973), we used the 275 disk-shaped reservoir described in Fjaer et al. (2008) with dimensions and physical properties defined above.

Figures 3 and 4 show cross-sections at $x = 0$ m of the displacement fields in 2D contour plots due to the pressure change in the whole cylindrical reservoir by using our methodology and Geertsma's method (Geertsma, 1973), respectively.

Because we defined the z -axis as positive downwards, the positive vertical displacement means a subsidence and the negative vertical displacement means an uplift. Figure 3 shows the horizontal and vertical displacements calculated, respectively,

280 with equations 23 and 25 by our methodology that uses the closed expressions of the full integrations (equations 24 and 25) of Nagy et al. (2000) and Nagy et al. (2002) (equations 26 – 35).

Figure 4 shows the radial and vertical displacements using Geertsma's method (Geertsma, 1973) considering an elastic homogeneous cylindrical reservoir under uniform depletion based on the nucleus-of-strain concept in the half-space, which in turn was proposed by Mindlin and Cheng (1950) and Sen (1951) in the theory of thermoelasticity.

285 In both cases (Figures 3b and 4b) the vertical displacements due to the entire the disk-shaped reservoir display a subsidence (positive values) above the reservoir and an uplift (negative values) below the reservoir. We stress that the proposed volume integrations (equations 26 – 35) allowed to evaluate the vertical displacement (Figure 3b) throughout the entire reservoir including inside and outside the reservoir. Rather, the vertical displacement using Geertsma's method (Figure 4b) is only valid outside the reservoir.

290 The radial displacement using Geertsma's method (Figure 4a) shows positive values at the edges of the reservoir ($y = -500$ and $y = 500$) with a singularity at the center of the reservoir ($x = 0$, $y = 0$ and $z = 800$ m). The horizontal displacement with the proposed full integration (Figures 3a) shows positive values at the edges of the reservoir ($y = -500$ and $y = 500$); however, it does not present singularities inside the reservoir.

295 Figure 5 shows the x -component displacement and vertical displacement by our methodology that uses a full volume integrations. These displacements are calculated along the x -axis, at $y = 0$ m and considering four surfaces located at the following depths: seafloor ($z = 0$ m), reservoir top ($z = 750$ m), reservoir center ($z = 800$ m) and reservoir bottom ($z = 850$ m). In the x -component of the displacement (Figure 5a), we can note an increased horizontal contraction from the center of the reservoir ($x = 0$) toward the reservoir edge ($x = 500$ m) where the maximum contraction of all surfaces occur. In the vertical displacement (Figure 5b), we can note a subsidence of the seafloor and the reservoir top (positive values) and an uplift of the 300 reservoir bottom (negative values). The vertical displacements of the seafloor, the top and bottom of the reservoir for Geertsma's method (Figure 6) show a similar behavior of those obtained by our methodology that uses a full volume integrations (Figure 5b). However, we note that the subsidence of the seafloor is more attenuated in the Geertsma's method than in our method. This fact is important because the movement of the seafloor should be monitored in hydrocarbon fields under production.

Figure 7 shows the null stress through the free surface at the plane $z = 0$ m due to reservoir under uniform depletion.

305 4.0.2 Disk-shaped reservoir under non uniform depletion

Here, we kept the same dimensions of the cylindrical reservoir simulated previously. We also kept the reservoir properties, except the pressure. We simulated a non-uniform depletion scenario where the cylindrical reservoir is composed by two vertically juxtaposed cylinders, each one with a uniform depletion. The deepest cylinder is uniformly depleted by $\Delta p = -20$ MPa with its top and bottom at, respectively, 800 and 850 m deep. The shallowest cylinder is uniformly depleted by $\Delta p = -40$ MPa with 310 its top and bottom at, respectively, 750 and 800 m deep.

We discretized the cylinders along the x -, y - and z - directions into an $20 \times 20 \times 2$ grid of prisms. This simulation totalized 800 prisms whose thicknesses are 50 m. The 400 deepest prisms are centered at 825 deep, with pressure contrast equal to -20 MPa and the 400 shallowest prisms are centered at 775 deep, with pressure contrast equal to -40 MPa

We calculate the displacement fields due to the pressure change in the whole cylindrical reservoir under non uniform depletion.
315 Figure 8 shows cross-sections at $x = 0$ m of the horizontal and vertical displacements, in 2D contour plots, calculated in the whole reservoir by using our methodology. Figure 9 shows the x -component displacement and vertical displacement that are calculated by our methodology along the x -axis, at $y = 0$ m and considering four surfaces located at the following depths: seafloor ($z = 0$ m), reservoir top ($z = 750$ m), reservoir center ($z = 800$ m) and reservoir bottom ($z = 850$ m).

By comparing Figure 8 with Figures 3, we can note similar behaviours of the displacement fields. However, the displacement
320 fields of reservoir under non uniform depletion (Figure 8) attain higher values because the higher variation of the pressure in the whole cylindrical reservoir.

In general, the displacements on the seafloor, the top, the center and the bottom of the reservoir under non uniform depletion
325 (Figure 9) show similar behaviors to the corresponding surfaces of the reservoir under uniform depletion (Figure 5). However, we can note higher displacements of these surfaces in the reservoir under non uniform depletion (Figure 9) due to the higher variation of the pressure in the whole cylindrical reservoir. Moreover, we can observe that the x -component displacements (Figure 9a) produced by the top (black line) and the bottom (red line) of the reservoir under non uniform depletion are not coincident to each other and the vertical displacement on the center of the reservoir under non uniform depletion (blue line in (Figure 9b) varies along the x -axis. Finally, we stress that the subsidence on the seafloor due to the reservoir under non uniform depletion (green line in Figure 9b) attains higher values (close to 20 cm) than the subsidence of the seafloor due to the
330 reservoir under uniform depletion (green line in Figure 5b).

We verify that the zero stress condition is satisfied at the free surface due to reservoir under a non uniform depletion as shown in Figure 10.

4.0.3 Reservoir with arbitrary geometry and under arbitrary pressure changes

In this numerical application, the reservoir model is a simplification of a realistic reservoir located in a production oil field in
335 offshore Brazil. The entire reservoir model comprises dimensions of 14 km in the north-axis, 13 km in the east-axis, and 0.6 km in the down-axis. The depths to the top and bottom of the reservoir model are 2,712 m and 3,312 m, respectively. The components of the displacements are calculated at 0 m deep, on a regular grid of 100×80 observation points along the north- and east-directions, respectively. We discretized the reservoir along the x -, y - and z - directions into an $14 \times 13 \times 2$ grid of prisms. The Young's modulus is 3300 (in MPa), the Poisson's coefficient is 0.25, and the uniaxial compaction coefficient C_m
340 (equation 13) is $2.2525 \cdot 10^{-4}$ MPa $^{-1}$. In the 3D perspective view of the pore pressure distribution of the simulated reservoir shown in Figure 11, we can see that the pressures vary from 0 to -0.72 MPa. Figure 12 shows cross-sections at $x = 8$ km of the horizontal and vertical displacements, in 2D contour plots, calculated in the whole reservoir by using our methodology. Figure 13 shows the null stress through the free surface due to reservoir with arbitrary geometry and under arbitrary pressure distribution.

Grounded on the similarity between the gravitational potential produced by a volume source under a density variation and the displacement field produced by a volume source in a half-space under a pressure variation, we have presented the analytical solution for the displacement field due to reservoir compaction with arbitrary geometry and under non-uniform pressure distribution. Our approach calculates the displacement field due to a reservoir by approximating its 3D pressure distribution through
 350 a piecewise constant function defined on a user-specified grid of 3D vertical prisms juxtaposed in the x -, y - and z -directions. By using the nucleus of strain as an infinitesimal volume element for each prism, we have calculated the displacement solution yielded by each prism through a 3D integration over the prism volume. The sum of the displacements produced by the prisms is the final displacement field due to the whole reservoir. The adopted exact analytical formulae, based on the gravitational field, to carry out the full integrations and calculate the displacement field due to reservoir compaction are valid expressions
 355 either outside or inside the prisms because the implemented expressions make use of modified arctangent function. We have demonstrated the use of these exact analytical expressions by applying them to calculate the displacement fields due to cylindrical reservoirs with uniform and non-uniform pressure distributions and to realistic reservoir model of a production oil field in offshore Brazil with arbitrary geometry and under arbitrary pressure distribution. All the numerical applications produced null stress fields at the free surface showing that the condition of null tractions at the free surface has been met. We have
 360 presented routines written in Python language (Python 3.7.6) to calculate the displacement and stress fields due to a reservoir with arbitrary shape and non-uniform distribution of pressure changes. The numerical applications and figures showing the results in this article were produced in Jupyter Notebook.

Code and data availability. The current version of our code is freely distributed under the BSD 3-clause licence and it is available for download at Zenodo: <http://doi.org/XXXXXXXX>. The latest development version of our code can be freely downloaded from a repository on
 365 GitHub (<https://github.com/pinga-lab/DisReserv>). Instructions for running the current version of our code are also provided on the repository. The code is still being improved and we encourage the user to work with the latest development version. The code was developed as an open-source Python language (Python 3.7.6). The numerical applications were produced in Jupyter Notebook. The data of the pore pressure distribution simulating a realistic reservoir (*realistic-model.pickle*) are available in the above-mentioned repositories.

Author contributions. VCFB and VCOJr deduced the equations in this paper. VCFB and ADA implemented the numerical applications
 370 presented in this paper. Most of the python codes were developed by VCOJr with some participation of VCFB. All authors contributed to the writing of the paper.

Competing interests. The authors declare that they have no conflict of interest.

Acknowledgements. Andre D. Arelaro thanks Petrobras, especially, the Multiphysics Group. Valeria C.F. Barbosa was supported by fellowships from: CNPq (grant 307135/2014- 4) and FAPERJ (grant E-26/202.582/2019). Vanderlei C. Oliveira Jr. was supported by fellowships

375 from: CNPq (grant 308945/2017-4) and FAPERJ (grant E-26/202.729/2018).

Financial support. This work is supported by the Brazilian research agencies Conselho Nacional de Desenvolvimento Científico e Tecnológico (CNPq) and Fundação Carlos Chagas Filho de Amparo à Pesquisa do Estado do Rio de Janeiro (FAPERJ).

References

- Beltrami, E.: Opere Matematiche, Hoepli, Milano, 1902–1920.
- 380 Borges, F., Landro M., and Duffaut, K.: Time-lapse seismic analysis of overburden water injection at the Ekofisk field, southern North Sea, GEOPHYSICS, 85, B9–B21, 2020
- Dahm, T., Cesca, S., Hainzl, S., Braun, T., and Krüger, F.: Discrimination between induced, triggered, and natural earthquakes close to hydrocarbon reservoirs: A probabilistic approach based on the modeling of depletion-induced stress changes and seismological source parameters, J. Geophys. Res. Solid Earth, 120, 2491–2509, 2015.
- 385 Faer, E., Holt, R. M., Horsrud, P., Raaen, A.M., and Risnes, R.: Petroleum related rock mechanics: Elsevier, 53, 2008.
- Fukushima, T.: Speed and accuracy improvements in standard algorithm for prismatic gravitational field, Geophys. J. Int., 222, 1898–1908, 2020.
- Geertsma, J.: A remark on the analogy between thermoelasticity and the elasticity of saturated porous media. J. Mech. Phys. Solids, 6, 13–16, 1957
- 390 Geertsma, J.: Problems of rock mechanics in petroleum production engineering, in: Proc. First Cong. Int. Soc. Rock Mech., 1, 585–594, 1966.
- Geertsma, J.: Land Subsidence above compacting oil and gas reservoirs, J. Pet. Tech. 25, 734–744, 1973.
- Geertsma, J., and van Opstal, G.: A numerical technique for predicting subsidence above compacting reservoirs, based on the nucleus of strain concept," Verhandelingen Kon. Ned. Geol. Mijnbouwk., 28, 63–78, 1973.
- 395 Goodier, J. N.: On the Integration of the Thermo-elasti equations, Phil. Mag. 7, 1017-1032, 1937.
- Grigoli, F., Cesca, S., Priolo, E., Rinaldi, A.P., Clinton, J.F., Stabile, T.A., Dost, B., Fernandez, M.G., Wiemer, S. and, Dahm T.: Current challenges in monitoring, discrimination, and management of induced seismicity related to underground industrial activities: a European perspective, Rev. Geophys., 55, 310–340, 2017
- Kellogg, O. D.: Foundations of Potential Theory, rederick Ungar Publishing Company, 1929.
- 400 Mehrabian, A., and Abousleiman, Y.A.: Geertsma's subsidence solution extended to layered stratigraphy, J. Pet. Sci. Eng., 130, 68–76, 2015.
- Mindlin, R.D. and Cheng, D.H.: Thermoelastic stress in the semi-infinite solid, J. Appl. Phys. 21, 931–933, 1950.
- Muñoz, L.F.P. and Roehl, D: An analytical solution for displacements due to reservoir compaction under arbitrary pressure changes, Appl. Math. Modell., 52, 145–159, 2017.
- Nagy, D., Papp, G., and Benedek, J.: The gravitational potential and its derivatives for the prism: Journal of Geodesy, 74, 552–560, 2000.
- 405 Nagy, D., Papp, G., and Benedek, J.: Corrections to "The gravitational potential and its derivatives for the prism": Journal of Geodesy, 76, 475, 2002.
- Segall, P.: Induced stresses due to fluid extraction from axisymmetric reservoirs. Pure Appl. Phys. 139, 536–560, 1992.
- Sen, B.: Note on the Stresses Produced by Nuclei of Thermoelastic Strain in a Semi-infinite Solid, Quart. Appl. Math., 8, 365–369, 1951.
- Sharma, B.D.: Stresses in an infinite slab due to a nucleus of thermoelastic strain in it, Z. Angew. Math. Mech., 36, 565–589, 1956.
- 410 Tao, L.N: Integration of the dynamic thermoelastic equations, Int. J. Eng. Sci., 9, 489–505, 1971
- Tempone, P., Fjaer, E., and Landro, M.: Improved solution of displacements due to a compacting reservoir over a rigid basement, Appl. Math. Modell. 34, 3352–3362, 2010.
- Tempone, P., Landro, M., and Fjaer, E.: 4D gravity response of compacting reservoirs: Analytical approach, Geophysics, 77, G45–G54, 2012.

van Thienen-Visser, K. and Fokker, P. A.:The future of subsidence modelling: compaction and subsidence due to gas depletion of the

415 Groningen gas field in the Netherlands, 96, Netherlands Journal of Geosciences, 96, s105–s116, 2017.

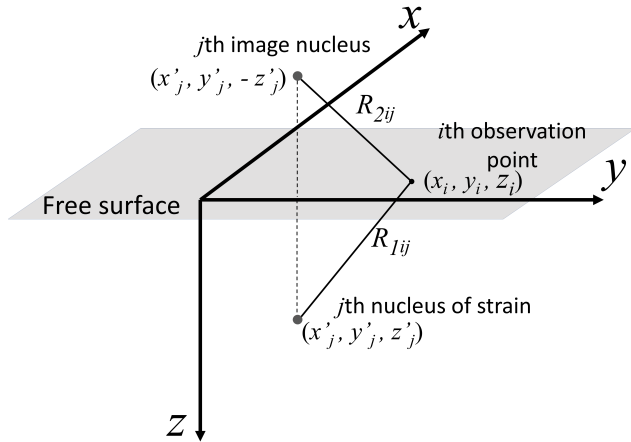


Figure 1. Schematic representation of the geometry of the nucleus of strain in a semi-infinite medium. After Muñoz and Roehl (2017). The adopted Cartesian coordinate system considered the x -axis pointing to north, the y -axis pointing to east and the z -axis pointing downward.

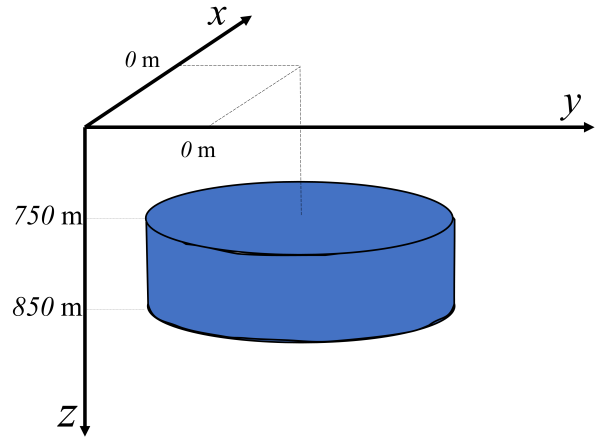


Figure 2. Disk-shaped reservoir under uniform depletion with a radius of 500 m

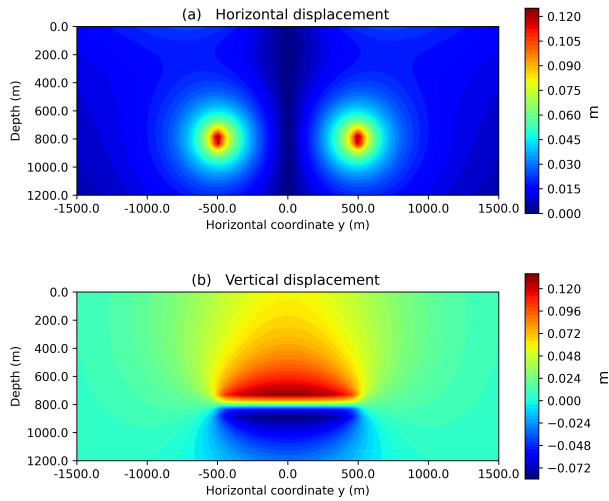


Figure 3. Reservoir under uniform depletion: (a) Horizontal displacement (equation 23) and (b) vertical displacement (equation 25) by our methodology that uses the closed expressions of the volume integrations given by Nagy et al. (2000) and Nagy et al. (2002) (equations 26-35)

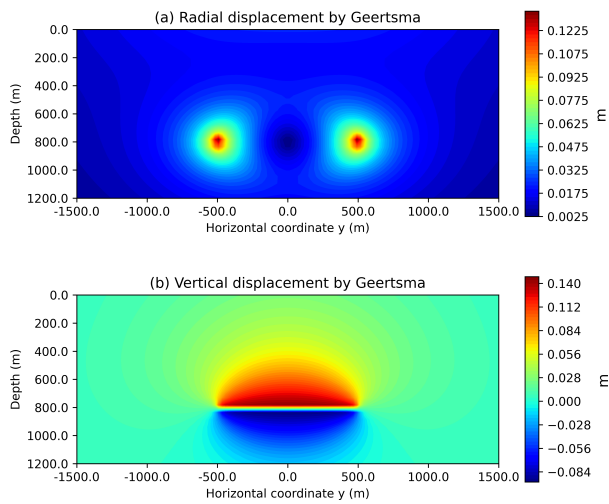


Figure 4. Reservoir under uniform depletion: (a) Radial displacement and (b) vertical displacement using Geertsma's method (Geertsma, 1973) considering an elastic homogeneous cylindrical reservoir under uniform depletion (Fjaer et al., 2008)

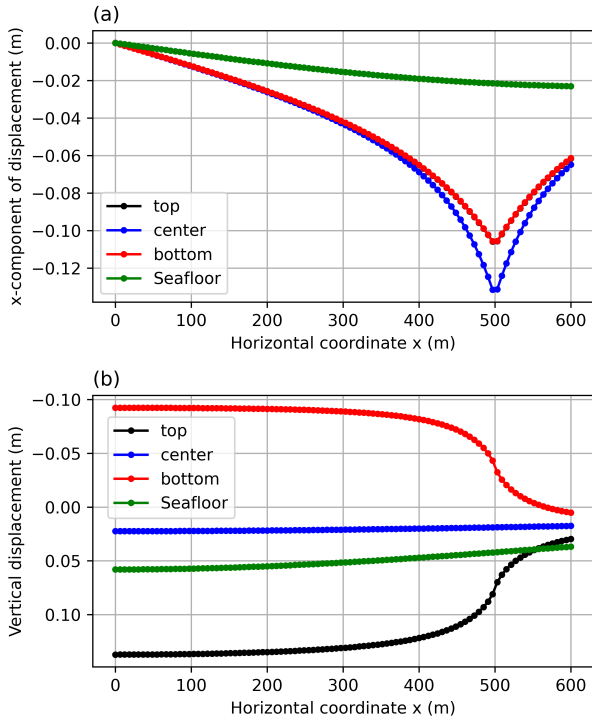


Figure 5. Reservoir under uniform depletion: (a) Horizontal x-component displacement and (b) vertical displacement by our methodology that uses the closed expressions of the volume integrations given by Nagy et al. (2000) and Nagy et al. (2002) (equations 26-35). These displacements are calculated along the x-axis, at $y = 0$ m and z located at the depths of: seafloor ($z = 0$ m), reservoir top ($z = 750$ m), reservoir center ($z = 800$ m) and reservoir bottom ($z = 850$ m).

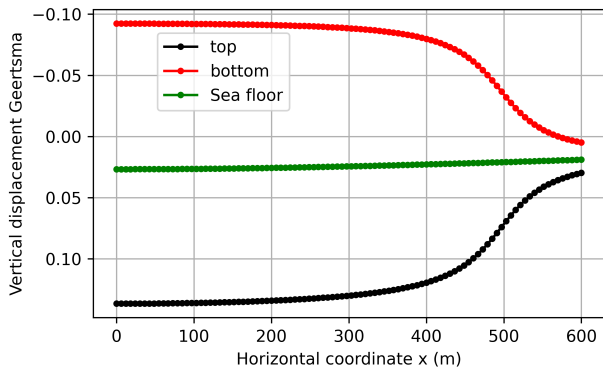


Figure 6. Reservoir under uniform depletion: Vertical displacement using Geertsma's method (Geertsma, 1973) considering an elastic homogeneous cylindrical reservoir under uniform depletion (Fjaer et al., 2008). The displacement is calculated along the x-axis, at $y = 0$ m and z located at the depths of: seafloor ($z = 0$ m), reservoir top ($z = 750$ m), and reservoir bottom ($z = 850$ m).

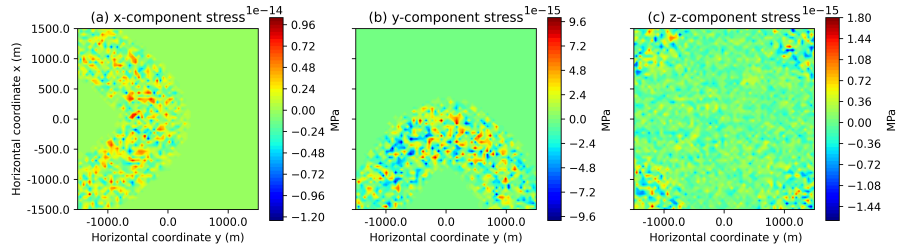


Figure 7. Reservoir under uniform depletion: (a) x –, (b) y –, and (c) z –components of the stress at the free surface.

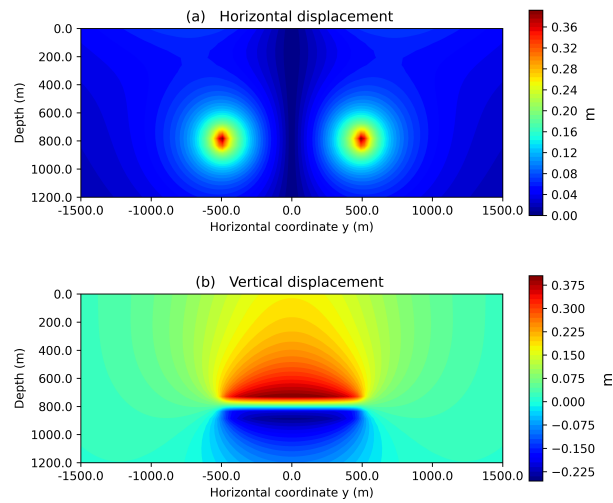


Figure 8. Reservoir under non uniform depletion: (a) Horizontal displacement (equation 23) and (b) vertical displacement (equation 25) by our methodology that uses the closed expressions of the volume integrations given by Nagy et al. (2000) and Nagy et al. (2002) (equations 26–35)

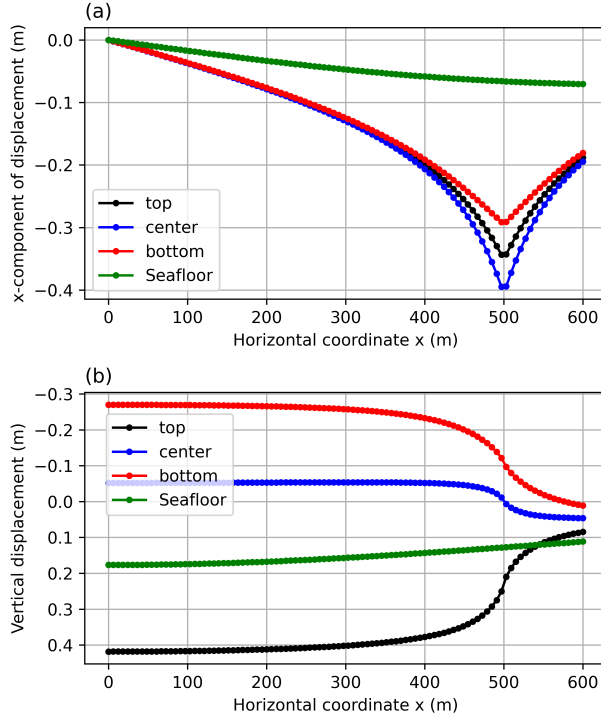


Figure 9. Reservoir under non uniform depletion: (a) Horizontal x-component displacement and (b) vertical displacement by our methodology that uses the closed expressions of the volume integrations given by Nagy et al. (2000) and Nagy et al. (2002) (equations 26–35). These displacements are calculated along the x-axis, at $y = 0$ m and z located at the depths of: seafloor ($z = 0$ m), reservoir top ($z = 750$ m), reservoir center ($z = 800$ m) and reservoir bottom ($z = 850$ m).

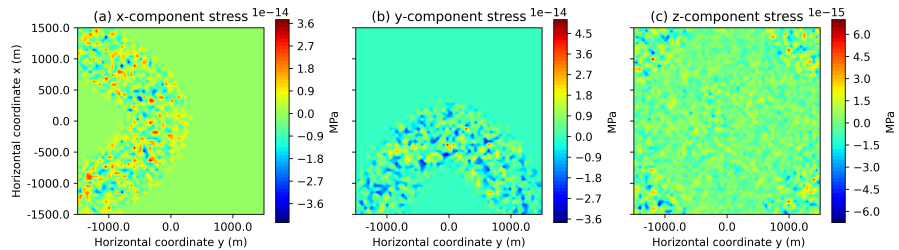


Figure 10. Reservoir under non uniform depletion: (a) x –, (b) y –, and (c) z –components of the stress at the free surface.

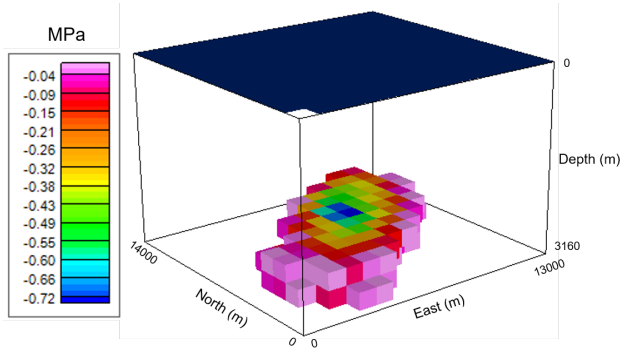


Figure 11. Reservoir with arbitrary geometry and under arbitrary pressure changes: 3D perspective view of the pore pressure distribution of a realistic reservoir located in a production oil field in offshore Brazil.

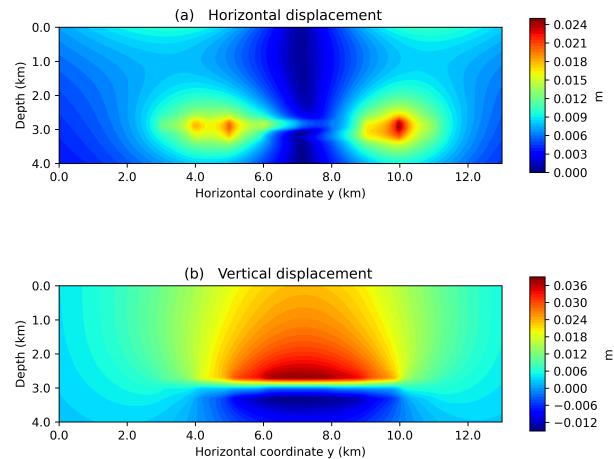


Figure 12. Reservoir with arbitrary geometry and under arbitrary pressure changes: (a) Horizontal displacement (equation 23) and (b) vertical displacement (equation 25) by our methodology that uses the closed expressions of the volume integrations given by Nagy et al. (2000) and Nagy et al. (2002) (equations 26–35)

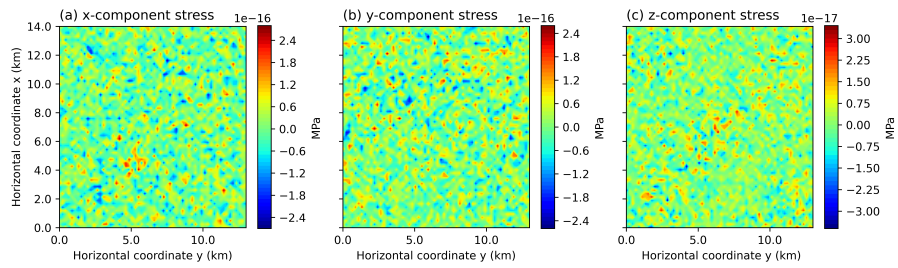


Figure 13. Reservoir with arbitrary geometry and under arbitrary pressure changes: (a) x –, (b) y –, and (c) z –components of the stress at the free surface.